To cite this article: LIU K, CAO L S, WAN D C. Suppression of tip vortex cavitation of elliptical hydrofoil based on active water injection methods[J/OL]. Chinese Journal of Ship Research, 2023, 18(4). http://www.ship-research.com/en/article/doi/10.19693/j.issn.1673-3185.02868.

DOI: 10.19693/j.issn.1673-3185. 02868

Suppression of tip vortex cavitation of elliptical hydrofoil based on active water injection methods

LIU Kang[1,2], *CAO Liushuai*[1,2], *WAN Decheng*[*1,2]

1 Computational Marine Hydrodynamics Lab, Shanghai Jiao Tong University, Shanghai 200240, China
2 School of Naval Architecture, Ocean and Civil Engineering, Shanghai Jiao Tong University, Shanghai 200240, China

Abstract: [**Objective**] As tip vortex cavitation (TVC) causes noise radiation and vibration, it is necessary to understand how to predict and control its development, and understand its mechanism in order to suppress it, especially in the field of ship propellers and other rotating machinery. [**Method**] Focusing on an elliptical hydrofoil with a NACA 0012 cross-section, this study uses the Improved Delayed Detached Eddy Simulation (IDDES) turbulence modeling method and Schnerr−Sauer cavitation model to simulate TVC on the hydrofoil and analyze its behavioral characteristics under wet flow and cavitation flow conditions. After that, two active water injection methods, side injection and top injection, are introduced into the simulation to reduce and suppress cavitation inception respectively. [**Results**] Taking the cavity volume of the tip vortex as the criterion for cavitation suppression, compared with the condition without water injection, top injection can inhibit cavitation by 8.09%. Moreover, under the condition of side injection, the effect of the injecting flow on the cavitation is more obvious, reaching 10.47%. The results show that both top and side injection can effectively suppress TVC. [**Conclusion**] Top injection can change the flow direction and speed of the tip vortex incident flow, and increase the dissipation term of the turbulent kinetic energy; while in side injection, the energy it carries acts directly on the vortex structure of the hydrofoil, destroying the vortex and greatly suppressing the generation of cavitation.

Key words: elliptical hydrofoil; active water injection; tip vortex cavitation; IDDES; Schnerr−Sauer

CLC number: U661.1

0 Introduction

Cavitation is a common physical phenomenon that occurs during the operation of hydraulic machinery. Specifically, the pressure decreases due to the acceleration of the wake field by hydraulic machinery during its operation, and cavitation occurs when the pressure drops to the saturated vapor pressure at the local temperature [1]. Tip vortex cavitation (TVC) is a special type of cavitation common in the operation of propellers or elliptical hydrofoils [2]. Tip vortex cavities do not attach to the propeller or hydrofoil surfaces during their generation and development. As a result, they will not have a significant influence on the propulsion efficiency of the propellers and hydrofoils, neither will they produce excessive corrosion. However, the development of tip vortex cavities often entails a process of collapse, which may increase the pressure fluctuation in the local

Received: 2022 − 04 − 24 **Accepted:** 2022 − 08 − 21

Supported by: National Natural Science Foundation of China (52001210, 52131102)

Authors: LIU Kang, male, born in 1999, master's degree candidate. Research interest: tip vortex cavitation inhibition. E-mail: 18754095981@163.com

CAO Liushuai, male, born in 1990, Ph.D., assistant researcher. Research interests: ship and ocean computational hydrodynamics, the wake of blunt body in stratified flow, and cavitation flow. E-mail: liushuaicao@sjtu.edu.cn

WAN Decheng, male, born in 1967, Ph.D., professor, doctoral supervisor. Research interests: computational ship hydrodynamics, grid-free particle method, ship shape optimization, fluid-structure interaction, and vortex-induced vibration/motion. E-mail: dcwan@sjtu.edu.cn

***Corresponding author:** WAN Decheng

flow field, cause flow-induced noise, and ultimately reduce the comfort of ships. For warships, noise can affect their concealment, making them less safe. Therefore, predicting and controlling the TVC phenomenon is vital.

In recent years, scholars have gained an increasingly mature understanding of tip vortices and TVC during their ongoing research on TVC. To determine the interaction between a tip vortex and TVC, Ji et al. [3] discussed the Delft Twist-11 hydrofoil as an example. By analyzing the proportion of each component in the vorticity transport function of the tip vortex, they found that the expansion term concerning the tip vortex increased significantly during cavitation, with its amplitude reaching the same level as that of the eddy-related stretching term. In contrast, the value of this term was zero under the wetted flow condition. Therefore, they concluded that the influence of cavitation on the tip vortex was mainly reflected in the expansion term. Coincidentally, Cheng et al. [4] came to the same conclusion when simulating the tip leakage vortex generated by a NACA 0009 hydraulic hydrofoil by the large eddy simulation (LES) method. Ohta et al. [5] simulated the cavitation at the turbulent boundary layer under the condition of Re = 2 000−2 600 to study the influence of TVC on the tip vortex flow. The results showed that the cavities blocked the exchange of the turbulent kinetic energy between fluids when cavitation occurred, reducing the transfer of momentum flowing to other directions. Kuiper et al. [6] used a Doppler laser tester to measure the velocity field near the fully developed vortex cavitation region. They observed that cavitation only affected the nearby flow domain while the velocity of the fluid far from the cavitation region was similar to that in the non-cavitating state. In addition, compared with the tip vortex flow in the non-cavitating state, the fluid had an azimuthal velocity that decreased near the cavitation interface and reached its maximum at a specific distance from the cavitation edge.

Scholars have proposed a number of flow control methods to suppress TVC and reduce the harm of tip vortex cavities. Those methods are divided into passive and active control ones [7]. Passive control involves influencing the flow field near the cavitation region by optimizing the external structure of the equipment [8]. In contrast, active control involves interfering with the pressure and velocity distribution of the flow field near the cavitation region by means of water injection. Although both the two types of methods can effectively suppress cavities, the latter also allows easy adjustment in different working environments. Currently, the active control method has become a popular solution to the cavitation behind hydrofoils and propellers. For example, Wang et al. [9] numerically simulated the hole opening and water injection of the NACA 0066 hydrofoil and then compared the results with the experimental values. The results showed that water injection effectively reduced the cavitation area on the suction side of the hydrofoil blades and also effectively lowered the drag on the hydrofoil in addition to ensuring the lift performance. Chang et al. [10] found that the development of TVC could be effectively suppressed by injecting water or water-based polymers into the core of the tip vortex. They also observed that the introduction of water injection significantly reduced the flow instability in the vortex core region. Timoshevskiy et al. [11] studied the influence of tangential water injection on the suction side of the hydrofoil by combining experimental and numerical methods. The results revealed that tangential water injection effectively reduced the area of sheet cavitation and that sheet cavitation has been effectively suppressed, which further verified the effectiveness of water injection for cavity control. Lu et al. [12] conducted hole opening and water injection on the suction side of the NACA 0066 hydrofoil, efficiently suppressing the sheet and cloud cavitation of hydrofoils. Lee et al. [13] experimentally applied water injection to elliptical hydrofoils and propellers to explore the influence of water injection on TVC and further analyze the TVC noise. The results showed that cavitation was markedly suppressed by water injection. Moreover, faster water injection corresponded to a more obvious cavitation delay and smaller noise induced by cavities.

According to the existing literature, active water injection effectively reduces the length the TVC develops. However, the simulation of the suppression of hydrofoil tip vortex and its TVC by active water injection has rarely been reported so far. Moreover, the mechanism of cavity suppression by active water injection has not been clarified. In this study, the authors intend to use the improved delayed detached eddy simulation (IDDES) turbulence model and the Schnerr−Sauer cavitation

model to simulate the TVC of the NACA 0012 elliptical hydrofoil on STAR-CCM+. Furthermore, hole opening and water injection at two different positions are designed to control the TVC of the hydrofoil, study the interaction among water injection, hydrofoil tip vortex, and cavitation, and analyze the mechanism of cavitation suppression by active water injection.

1 Numerical method

1.1 Control equation

In the field of hydromechanics, mathematical models built in computational fluid dynamics (CFD) simulation are all based on the Navier−Stokes (N−S) equation. This equation describes the physical essence of many phenomena in the field of hydromechanics and mathematically explains the conservation of momentum and mass in Newtonian fluids [14]. The N−S equation for incompressible fluids is Eqs. (1) and (2).

$$\nabla \cdot \boldsymbol{V} = 0 \tag{1}$$

$$\frac{\partial \rho \boldsymbol{V}}{\partial t} + \nabla \cdot (\rho \boldsymbol{V}\boldsymbol{V}) = -\frac{(\nabla p)}{\rho} + \frac{\mu \nabla^2 \boldsymbol{V}}{\rho} \tag{2}$$

where ρ is the fluid density; p is the flow field pressure; μ is the viscosity coefficient; t is time; $\boldsymbol{V}$ is the velocity vector; the symbol " ∇ " is the parameter gradient; the symbol " $\nabla\cdot$ " is the parameter divergence; the symbol " ∇^2 " is the Laplace operator.

1.2 IDDES turbulence model

The N−S equation is the basis of CFD simulation. However, obtaining the accurate solution to flow field information merely by this equation requires huge computational resources, and this equation is only applicable to some simple scenarios. Therefore, scholars often simplify this equation according to different assumptions to obtain turbulence models when dealing with practical problems. Currently, the mainstream turbulence models include the direct numerical simulation (DNS) model, the large eddy simulation (LES) model, and the Reynolds-averaged Navier–Stokes (RANS) model.

Each of the three turbulence methods has its own advantages and disadvantages. Specifically, the RANS model has low requirements on computational resources and grid quality, but the errors in its calculation results are large; the LES model improves the calculation accuracy substantially by filtering the calculation results using a subgrid-scale model. Nevertheless, it places high requirements on grid accuracy, ultimately greatly prolonging the calculation cycle and reducing the computational economy; similarly, the DNS model suffers from the same problem as the LES model.

The IDDES model used in this study combines the advantages of the RANS and LES methods by reconstructing the subgrid-scale model in the LES model and using the RANS model near the wall whereas the LES model is used in other flow fields. In this way, the IDDES model not only ensures computational accuracy but also reduces the requirements on grid quality. It is thus widely used in the simulation of fine flow fields. Cao et al. [15] finely captured the coherent vortex structure near the sphere using the IDDES model. Wang et al. [16] used this turbulence model to simulate the flow field of a high-speed train. The above efforts both achieved favorable results. The IDDES equation [17] is expressed as Eqs. (3) to (5).

$$\frac{\partial \rho k}{\partial t} + \nabla \cdot (\rho k \boldsymbol{V}) = \nabla \cdot [(\mu + \sigma_k \mu_t)(\nabla k)] + P_k - \rho \sqrt{k^3}/l_{\mathrm{IDDES}} \tag{3}$$

$$\frac{\partial \rho \omega}{\partial t} + \nabla \cdot (\rho \omega \boldsymbol{V}) = \nabla \cdot [(\mu + \sigma_\omega \mu_t)(\nabla \omega)] + 2(1-F_1)\rho\sigma_{\omega 2}\frac{(\nabla k)\cdot(\nabla \omega)}{\omega} + \alpha \frac{\rho}{\mu_t} P_k - \beta \rho \omega^2 \tag{4}$$

$$\mu_t = \rho \frac{a_1 k}{\max(a_1 \omega, F_2 \boldsymbol{S})} \tag{5}$$

where k is the turbulent kinetic energy of the flow field; ω is the turbulent dissipation rate of the flow field; $\boldsymbol{S}$ is the strain-rate tensor; l_{IDDES} is the scale of turbulence under the IDDES model; F_1 and F_2 are mixed functions; P_k is the result term; σ_k, σ_ω, and $\sigma_{\omega 2}$ are model coefficients, and α, β, a_1 are calculated constants.

F_1, F_2, and P_k can be calculated from Eqs. (6) to (8).

$$F_1 = \tanh\left(\arg_1^4\right) \tag{6}$$

$$F_2 = \tanh\left(\arg_2^2\right) \tag{7}$$

$$P_k = \min\left(\mu_t \boldsymbol{S}^2,\ 10 C_\mu \rho k \omega\right) \tag{8}$$

where C_μ is the model coefficient. The relevant calculation equations for internal parameters have been detailed in Reference [17] and will thus not be repeated here.

1.3 Cavitation models

In the field of CFD, the cavitation in a flow field

is simulated using cavitation models. According to different theoretical methods, cavitation models are divided into state equation-based ones and transport equation-based ones. The Schnerr−Sauer cavitation model used in this study is based on a transport equation. Mathematically expresses the vaporization and condensation processes of fluids, this equation captures cavitation realistically [18].

Currently, the Schnerr−Sauer cavitation model has been embedded into multiple commercial CFD software, and verification results demonstrate that it fully meets the engineering requirements on accuracy. In the field of cavitation-related research, the Schnerr−Sauer cavitation model has often been employed by scholars. For example, Yilmaz et al. [19] simulated tip vortex cavities generated by propellers using the Schnerr−Sauer cavitation model. The comparison revealed small errors between simulation results and experimental values. Similarly, Giorgi et al. [20] studied the inception process of the initial TVC produced by hydrofoils with this model. The transport equation for the cavitation model [18] is expressed as Eq. (9).

$$\frac{\partial \alpha_v \rho_v}{\partial t} + \nabla \cdot (\alpha_v \rho_v \boldsymbol{V}) = \dot{m}_c + \dot{m}_v \tag{9}$$

where α_v is the proportion of the gas phase during cavitation; ρ_v is the gas phase density; $\dot{m}_c$ and $\dot{m}_v$ are the mass transfer terms during condensation and vaporization, respectively.

In the Schnerr−Sauer cavitation model, $\dot{m}_c$ and $\dot{m}_v$ are expressed as

$$\dot{m}_c = C_c \frac{3\rho_v \rho_l \alpha_v (1-\alpha_v)}{\rho R} \operatorname{sgn}(P_v) \sqrt{\frac{2|P_v - P|}{3\rho_l}} - C_c \frac{3\rho_v \rho_l \alpha_v (1-\alpha_v)}{\rho R} \operatorname{sgn}(P) \sqrt{\frac{2|P_v - P|}{3\rho_l}} \tag{10}$$

$$\dot{m}_v = C_v \frac{3\rho_v \rho_l \alpha_v (1-\alpha_v)}{\rho R} \operatorname{sgn}(P_v) \sqrt{\frac{2|P_v - P|}{3\rho_l}} - C_v \frac{3\rho_v \rho_l \alpha_v (1-\alpha_v)}{\rho R} \operatorname{sgn}(P) \sqrt{\frac{2|P_v - P|}{3\rho_l}} \tag{11}$$

$$R = \left(\frac{\alpha_v}{1-\alpha_v} \cdot \frac{3}{4\pi n_0} \right)^{1/3} \tag{12}$$

where C_c is the condensation model coefficient; C_v is the vaporization model coefficient; ρ_l is the liquid phase density; P_v is the liquid saturation pressure; P is the fluid pressure; R is the local bubble radius; n_0 is the density of the cavity seed.

2 Simulation calculation

2.1 Geometric model and computational domain

Since the currently available experimental data on the cavitation and hydrodynamic performance of the NACA 0012 elliptical hydrofoil is rather complete, this airfoil is adopted to simulate the TVC phenomenon of hydrofoils and further verify the turbulence and cavitation models used in this study. The geometric model of the NACA 0012 elliptical hydrofoil, as shown in Fig. 1(a), has a chord length C = 150 mm and a span S = 176.7 mm.

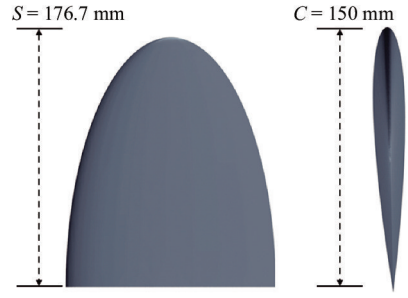

(a) Geometric model and principal dimensions of NACA 0012 elliptical hydrofoil

(b) Computational domain

Fig. 1 Geometric model of NACA 0012 elliptic hydrofoil and setting of computational domain

The chord length C of the NACA 0012 elliptical hydrofoil is taken as the unit of measurement for dimensions in the computational domain. Moreover, the flow direction and the span direction of the hydrofoil are taken as the x and z directions of the computational domain, respectively, and the remaining direction is taken as the y direction of the computational domain, corresponding to the length, height, and width of the computational domain, respectively. This computational domain is designed into the shape of a $16C \times 3C \times 3C$ cuboid bucket. The boundary of the computational domain should be as far away from the installation position of the hydrofoil as possible to better simulate the TVC of the hydrofoil and reduce the influences of the boundary, the inlet, and the outlet on the calculation results. Therefore, except for the placement of the hydrofoil at the bottom of the computational domain in the z direction according to the actual situation, the hydrofoil should be

located in the central area of the computational domain in both the x and y directions. The overall setting of the computational domain is shown in Fig. 1(b).

2.2 Grid division

In the process of fluid flow, the tip vortex and the cavitation structure therein will constantly roll over to form a minimal-scale vortex structure as the tip vortex develops backward. The flow inside the tip vortex changes dramatically, and even the small-scale disturbances generated in the calculation process will have a significant impact on the simulation results. Therefore, the grids at the position of the tip vortex in the computational domain need to be refined to accurately simulate the tip vortex and TVC generated by the hydrofoil. Since the tip vortex bends along the flow direction into a bow shape rather than being a standard cylindrical shape, refining the grids at the position of the tip vortex by the structured grid division method is difficult. In this study, the grids in the computational domain of the NACA 0012 elliptical hydrofoil are divided by applying the polyhedral grid division method and the volume refinement method in STAR-CCM+.

The basic grid size is set to 0.1C; the maximum grid size in the computational domain is 0.4C (approximately 0.06 mm); the surface grid size of the elliptical hydrofoil is 0.01C. To better capture the TVC generated by the hydrofoil, the authors build an 8C × 2C × 2C cuboid grid buffer layer centered on the hydrofoil and set the grid size to 0.25C. The grids obtained will serve as the initial grid for estimating the motion trend of the flow field and preparing an initial flow field around the hydrofoil. Then, the Q = 5 000 s^{-2} contour surface in the initial flow field is extracted to locate the grid refinement region in the hydrofoil tip vortex. In addition, a three-layer cylinder (outer, middle, and inner cylindric volume refinement regions) is built nearby for volume grid refinement, and the grid sizes are set to 0.02C, 0.01C, and 0.005C, respectively. Although the volume grid refinement based on a three-layer cylinder effectively captures the tip vortex pattern of the NACA 0012 elliptical hydrofoil, it fails to capture the TVC satisfactorily. Therefore, the authors build an irregular TVC refinement region around the hydrofoil tip vortex by leveraging the 3D-CAD function of STAR-CCM+ and then set the grid size to 0.001C.

The refinement region in the computational domain of the tip vortex is shown in Fig. 2(a). In the figure, the red rectangular box is the buffer-layer refinement region; the yellow cylinder is the outer cylindric volume refinement region; the green cylinder is the middle cylindric volume refinement region; the cyan cylinder is the inner cylindric volume refinement region; the black area is the TVC-oriented volume refinement region. In the grid division shown in Fig. 2(b), the boundaries of the 5-layer refined grids are defined in different colors, such as red for the buffer layer, yellow for the outer cylinder, blue for the middle cylinder, green for the inner cylinder, and black for the TVC. Furthermore, active water injection is simplified as the velocity inlet surface in this study. For this purpose, the process of the injected fluid flowing in the injection pipe is temporarily left aside, and the simulation of active water injection is achieved by defining the velocity inlet on the hydrofoil surface. In this case, the injection surface needs to be separated from the hydrofoil surface and then refined in the process of grid division (red:

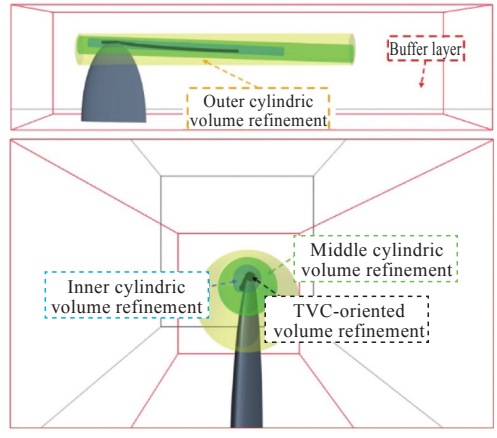

(a) Refinement position of computational domain

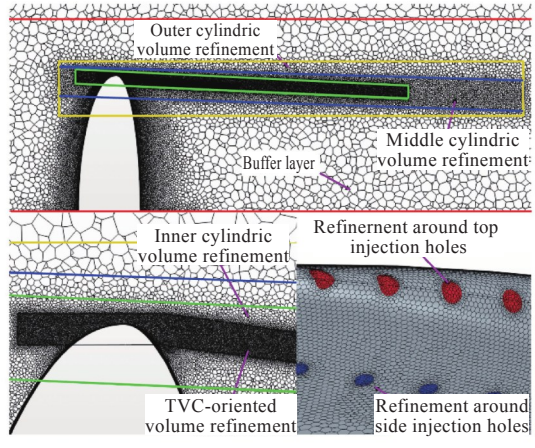

(b) Grid division of computational domain

Fig. 2 Refinement position and grid division of computational domain

refinement region for top injection; blue: refinement region for side injection) to a grid size of 0.001C. In addition, curve control is added at the edge of the injection surface to a curve size of 0.000 5C to keep the injection surface undeformed. The final number of grids is about 4 million.

2.3 Boundary conditions and discretization scheme

Regarding the computational domain, its inlet is set to a velocity inlet with an inflow velocity V_I = 6 m/s, and its outlet is set to a pressure outlet. The outlet pressure is set to the one under an open-water condition in the calculation of the lift coefficient; the outlet pressure P_∞ = 39 278 Pa in the simulation of cavitation, and the cavitation number σ_n = 2.01 in this case. The side boundary is set to a slip wall while the hydrofoil surface is set to a non-slip one.

For the conservation of computational resources during the calculation, a solver is set up for steady computation under open-water conditions, and the computation is assumed to be implicit unsteady under cavitation conditions. A second-order scheme is adopted for temporal discretization at a time step $\Delta t = 1\times10^{-5}$ s, with 20 iterations per time step. To ensure that the calculation reaches a stable state completely, Xie et al. [6] defined the stabilization time of the flow field as $10C/V_I$ and extended it by $2C/V_I$ for mathematical statistics when simulating the TVC of an elliptical hydrofoil. In this way, they obtained satisfactory numerical results. In the present study, the total calculation time of the simulation example under an unsteady condition is set to 0.30 s for the selected elliptical hydrofoil. Furthermore, the flow field information within 0.25–0.30 s is collected for time-averaged calculation. The curves of the lift/drag coefficient and the residual of the hydrofoil are monitored in the calculation process to determine the convergence of the solution.

2.4 Grid independence verification

Whether the currently available grid resolution meets the requirements of cavity prediction on accuracy is determined. For this purpose, grid independence is analyzed according to the grid independence verification specifications provided by the International Towing Tank Conference (ITTC) [19] and the refinement criteria for coarse (with a basic size of 0.03 m), medium (with a basic size of 0.021 2 m), fine (with a basic size of 0.015 m), and very fine (with a basic size of 0.010 6 m) grids. The final number of the four sets of grids is 0.70 million, 1.48 million, 3.72 million, and 8.41 million, respectively. Furthermore, the lift coefficient of the elliptical hydrofoil and the volume of the tip vortex cavity are selected as the analysis criteria for independence verification to further determine the accuracy of cavity prediction. The four sets of grids are shown in Fig. 3, and the simulation results are listed in Fig. 4.

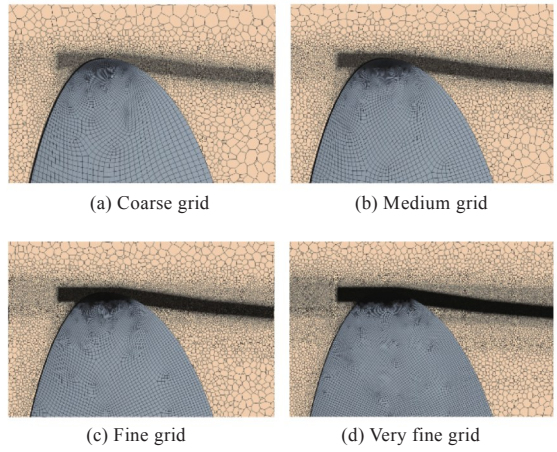

(a) Coarse grid (b) Medium grid

(c) Fine grid (d) Very fine grid

Fig. 3 Grid divisions for grid independence

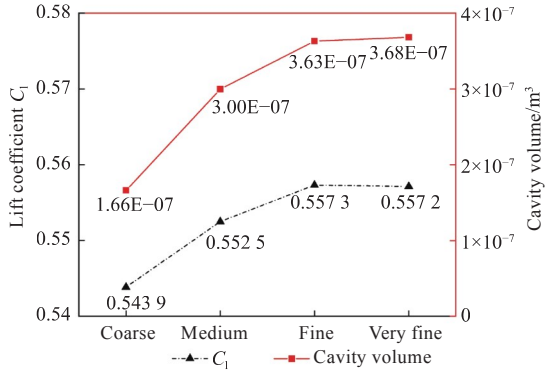

Fig. 4 Grid independence verification

The results show that both the lift coefficient and the cavity volume gradually converge when the grids are refined from coarse to very fine. The lift coefficient reaches its maximum at the fine level of the grids and then decreases when the grids are further refined to the very fine level. The total volume of the tip vortex cavities takes on an increasing trend as the refinement level of the grids rises, but the difference between its values at the fine and very fine levels of the grids is only 5×10^{-9} m^3. Comprehensively considering the requirements on computation period and accuracy, the authors select the fine level of grids for numerical calculation.

2.5 Model verification

Steady calculation of the lift coefficient of the NACA 0012 elliptical hydrofoil is conducted under wetted flow conditions to verify the correctness of the IDDES model. According to the trial results, the example tends to stabilize after 600 steps under steady conditions. In this study, the number of steps for the calculation of each condition is finally determined to be 1 000, and the lift coefficient of the elliptical hydrofoil is determined by averaging the calculation results within the range of 600 to 1 000 steps. Fig. 5 shows the variation in the lift coefficient of the NACA 0012 elliptical hydrofoil with the angle of attack α and compares the values with the experimental results from Takasugi et al. [21].

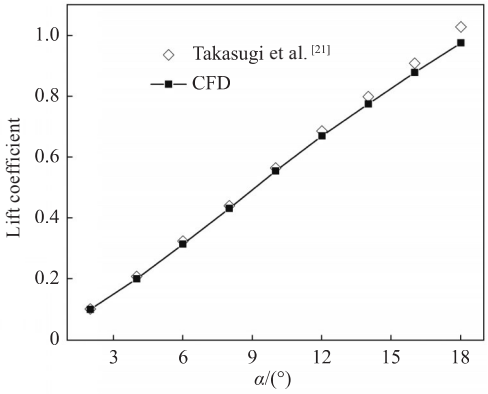

Fig. 5 Comparison between calculation and experimental results of lift coefficient

As can be seen from Fig. 5, the calculated lift coefficient of the NACA 0012 elliptical hydrofoil matches well with the experimental results, and they both demonstrate a linear growth trend as the angle of attack increases. Besides, the error between the simulation and experimental results increases up to 5.5% as the angle of attack grows because the flow in the computational domain becomes more turbulent. At an angle of attack α = 10°, the lift coefficients obtained by CFD simulation and experiments conducted by Takasugi et al. [21] are 0.585 and 0.565, respectively. Then, the error between them is 0.200, and the error rate is merely 3.54%, indicating that the IDDES model meets the engineering accuracy requirements.

After the calculation correctness of the IDDES turbulence model is verified, the form of the tip vortex cavities generated by the elliptical hydrofoil and the flow direction and velocity distributions at 90% span location in the far field (0.175 m away from the hydrofoil) under the condition of α = 10° are collected and compared with the experimental results from Takasugi et al. [21] to determine the interaction between the turbulence model and the Schnerr−Sauer cavitation model. Fig. 6 compares the numerical calculation results and experimental results [21] when the collected volume fraction of the tip vortex cavity α_v = 0.1.

As can be seen from Fig. 6(a), compared with the experimental results, the cavities obtained by the numerical method are attached to the surface of the elliptical hydrofoil. Nevertheless, the inception position and form of the tip vortex cavities are similar to the experimental results.

In Fig. 6(b), the horizontal axis is the y-direction coordinate and the vertical axis is the dimensionless velocity. This figure shows that the axial velocity at the 90% span location obtained by the numerical method is slightly smaller than the experimental results, which proves that a problem of high dissipation can be observed in the numerical results in the process of downstream flow. Nevertheless, the results match well with the experimental values overall, proving the applicability of the simulation method employed in this study.

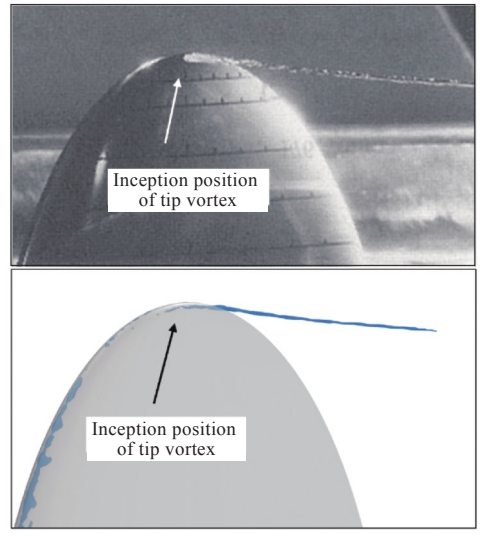

(a) Comparison of tip vortex form

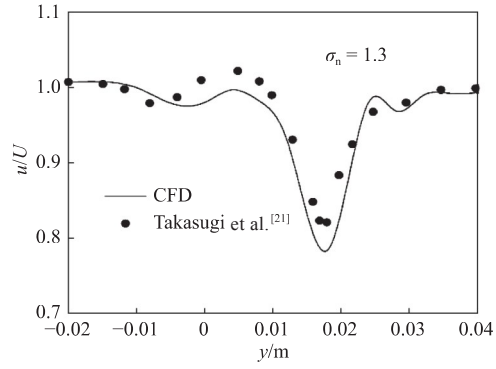

(b) Comparison of velocity distribution

Fig. 6 Comparison between CFD simulation and experimental results of hydrofoil

3 Results and analysis

3.1 Analysis of hydrofoil tip vortex and TVC characteristics

In this regard, the hydrofoil tip vortex and its cavitation are simulated under wetted flow and cavitating flow conditions to determine the changes in the tip vortex form and internal pressure before and after cavitation. Moreover, the motion of the flow field near the tip vortex is visualized, and the mechanism of hydrofoil TVC is analyzed. In this case, the angle of attack of the hydrofoil is α = 10°; the inflow velocity is V_I = 6 m/s; the cavitation number is σ_n = 2.01; the saturated vapor pressure of water is P_v = 3 170.34 Pa.

The tip vortex form of a hydrofoil can be identified according to the Q-Criterion:

$$Q = 0.5(\|\boldsymbol{\Omega}^2\| - \|\boldsymbol{S}^2\|) \tag{13}$$

where $\boldsymbol{\Omega}$ is the vortex tensor; the symbol "|| ||" is the computational symbol for norms.

Fig. 7 shows the hydrofoil tip vortices captured on the Q=5×10^5 s^{-2} contour plane under wetted flow and cavitating flow conditions. The tip vortex structure at x=0.1 m is enlarged to compare the influence of the tip vortex cavities on the hydrofoil tip vortex in a more clear way. Fig. 7 reveals no significant difference in the development trend of the hydrofoil tip vortex under the two conditions, with a downward bow-like shape of the trend in both cases. However, the enlarged tip vortex structure shows a significant difference in the shape of the vortex core under the two conditions. The vortex motion inside the hydrofoil vortex core is extraordinarily violent under the wetted flow condition, represented by the clear red color. In contrast, the vortex motion inside the hydrofoil tip vortex core slows down and the intensity of the vortex core significantly decreases under the cavitating flow condition. In addition, the shape of the tip vortex has also undergone significant changes. The hydrofoil tip vortex appears quasi-circular in the absence of cavitation and appears quasi-elliptical with an increased diameter after cavitation, which is particularly evident in Fig. 8.

The pressure contour and the flow velocity variation contour (Fig. 8) at x = 0.08 (near the TVC inception position) are collected to identify the causes of tip vortex and its cavitation.

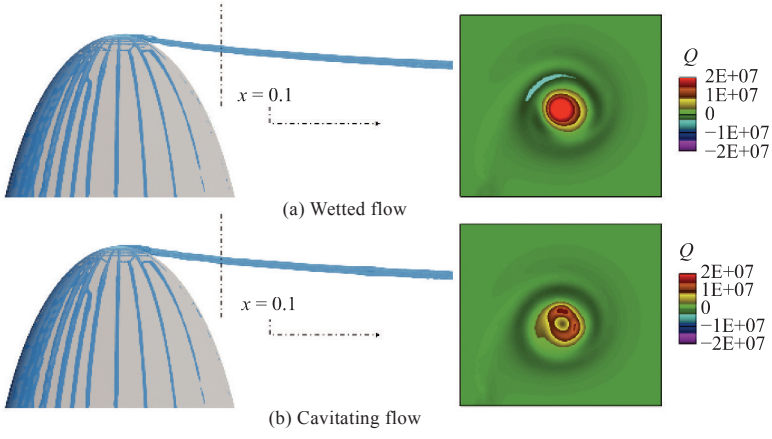

Fig. 7 Comparison between hydrofoil tip vortices in wetted flow and cavitating flow conditions

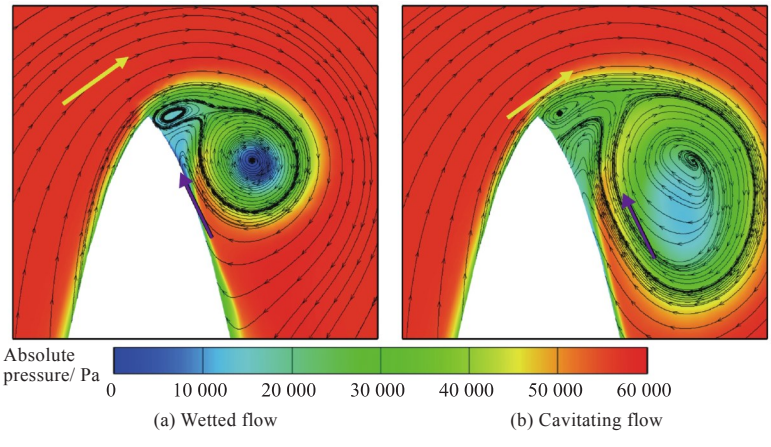

Fig. 8 Pressure contours of hydrofoil tip vortex at x = 0.08

According to Fig. 8, vortices are generated both at the tip and on the suction side of the hydrofoil under wetted flow conditions, and the tip vortices rotate violently with significant changes in the pressure gradient. A blue low-pressure region forms at the vortex core where the rotation is most intense, proving that the TVC originates from the swirling flow in the hydrofoil tip vortex. After cavitation occurs, a cavity is formed at the vortex core to compensate for the pressure in the low-pressure region, thereby reducing the pressure gradient inside the hydrofoil tip vortex; the decreased pressure gradient helps slow down the rotation of the hydrofoil tip vortex and ultimately lowers the intensity of the tip vortex.

According to the flow trend in Fig. 8, the fluid on the pressure side (left side) of the hydrofoil tends to move upward. When it passes the hydrofoil tip and reaches the suction side of the hydrofoil, the upward flow gradually bends under pressure and eventually converges near the suction-side surface of the hydrofoil to form a rotational flow. The rotation of the hydrofoil tip vortex can be divided into two parts on the basis of this flow trend: one is the incident flow from the pressure side of the hydrofoil (indicated by the yellow arrow); the other is the re-entrant flow converging to the suction side of the hydrofoil (indicated by the purple arrow).

3.2 Suppression effect of active water injection on hydrofoil TVC

After the flow trend and cavitation causes of the hydrofoil tip vortex are identified, an injection hole with a diameter of 1 mm is opened at the hydrofoil tip to control the development of TVC by the hole opening and water injection method. Specifically, the flow velocity of the injected fluid is 9 m/s, and the injected fluid is water, whose parameter setting is consistent with that of the environmental water. As shown in Fig. 9, the position of hole opening and water injection is divided into side hole opening and top hole opening according to the mode of action. Specifically, Fig. 9(b) shows the side hole opening, in which case the hole opening position is near the cavitation inception region and the injected fluid acts directly on the tip vortex; Fig. 9(c) shows the top hole opening, in which case the position is far from the tip vortex and its cavitation region to the effect that the injected fluid can only affect the tip vortex by influencing the motion of the flow field. The fluid is injected in the direction normal to the hole surface in the case of side pore opening, whereas the fluid is injected along the z direction in the case of top hole opening.

3.2.1 Hydrodynamic performance

The most important aspects of an elliptical hydrofoil as thrust machinery are lift and drag performance. In this study, the lift and drag coefficients of the hydrofoil surface under no injection (W/O), top injection (T/I), and side injection (S/I) conditions are measured. Fig. 10 shows the variations of the lift and drag coefficients over time under the three conditions. As can be seen from Fig. 10, side injection has little influence on the forces on the hydrofoil surface, and the fluctuation amplitude and period of the lift and drag coefficients under this condition are insignificantly different from those under the W/O condition. In contrast, top injection has a significant influence on the coefficients of the elliptical hydrofoil. For one thing, top injection increases the amplitudes of the fluctuations of the lift and drag coefficients over time, with an up to 0.01 maximum fluctuation amplitude of the lift coefficient and an up to 0.002 maximum fluctuation amplitude of the drag coefficient. For another, the lift performance and the drag coefficient on the hydrofoil surface under this condition are both slightly smaller than those under the W/O and S/I conditions. One of the primary causes for the vibration of the surface of hydrofoils and propellers is known to be the pressure fluctuation during cavity collapse [22]. Moreover, a more unstable cavity corresponds to a stronger excitation force. The increased amplitudes of the lift and drag coefficients on the hydrofoil surface under the T/I condition indicate that top injection not only effectively reduces the hydrofoil TVC but also reduces the stability of the tip vortex cavities, leading to an increase in the excitation force on the hydrofoil surface.

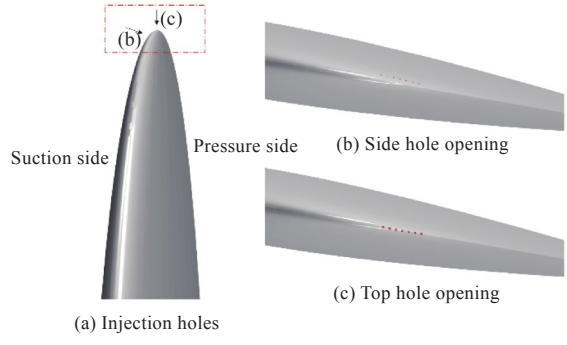

Fig. 9 Hole opening positions on hydrofoil

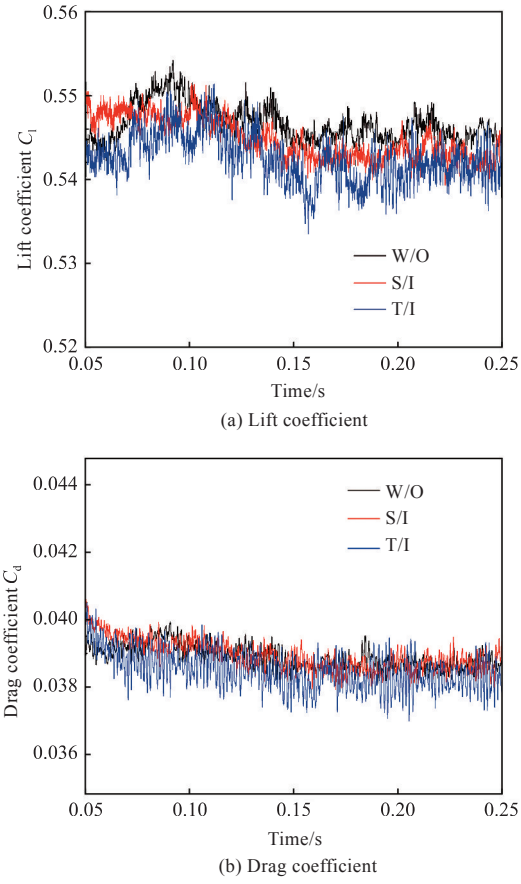

(a) Lift coefficient

(b) Drag coefficient

Fig. 10 Comparison of force coefficients under three water injection conditions

3.2.2 Cavity form

The length the hydrofoil TVC develops in the cases of the two hole opening methods is compared in Fig. 11, and the cavity volume is shown in Table 1. According to Fig. 11, the tip vortex cavities generated by the hydrofoil are structurally stable under the W/O condition and are in a columnar form. When hole opening and water injection are conducted, the two hole opening and water injection methods both effectively reduce the length the tip vortex cavities develops on the one hand; on the other hand, unlike side injection, top injection does not suppress the tip vortex cavities completely. A small number of cavities are continuously generated at the inception position under this condition, causing the tip vortex cavities to collapse ahead of the expected position. Consequently, the pressure fluctuates more violently on the hydrofoil surface, ultimately leading to an increase in the excitation force. The comparison with the results in Table 1 shows that side injection can suppress tip vortex cavitation by 10.47% under a constant injection velocity, and the tip vortex cavities generated by the hydrofoil almost disappear. In contrast, top injection suppresses cavities by 8.09%, representing an obvious but still inferior suppression effect to the former. Surely, both the two hole opening and water injection methods, especially side injection, effectively reduce the length the tip vortex cavity generated by the hydrofoil develops.

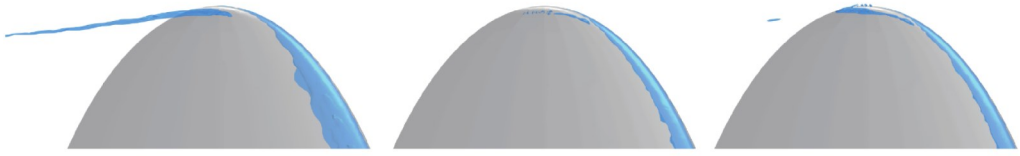

(a) W/O (b) S/I (c) T/I

Fig. 11 Comparison of cavity forms under three water injection conditions

Table 1 Influence of injection position on suppression of hydrofoil TVC

Injection position	Injection velocity /(m·s^{-1})	Cavity volume/m^3	Original cavity volume/m^3	Suppression rate/%
Side	9	3.25×10^{-7}	3.63×10^{-7}	10.47
Top	9	3.40×10^{-7}	3.63×10^{-7}	8.09

3.2.3 Flow field around tip vortex

According to the flow field analysis in Section 3.1, hydrofoil TVC can be attributed to the pressure drop caused by the swirling flow in the hydrofoil tip vortex. Thus, an effective means to analyze the suppression effect of water injection on cavitation is studying the influence of water injection on tip vortex motion. In this study, the section normal to the x direction at the center of an injection hole is extracted, and the influences of water injection on the flow trend and structure of the hydrofoil tip vortex are analyzed using the Q-Criterion contour and the streamlines in the local flow domain of the injection hole. The results are shown in Fig. 12.

Specifically, the inception position and development status of the hydrofoil tip vortex are identified under the W/O condition. As shown in Fig. 12(a), the hydrofoil tip vortex remains at an inception stage at x = 0.073. In this case, the tip vortex is small and close to the suction-side surface of the hydrofoil. In contrast, the hydrofoil tip vortex has developed into its full form at x = 0.082. Then, the interference effects of the two water injection methods on the hydrofoil tip vortex are determined.

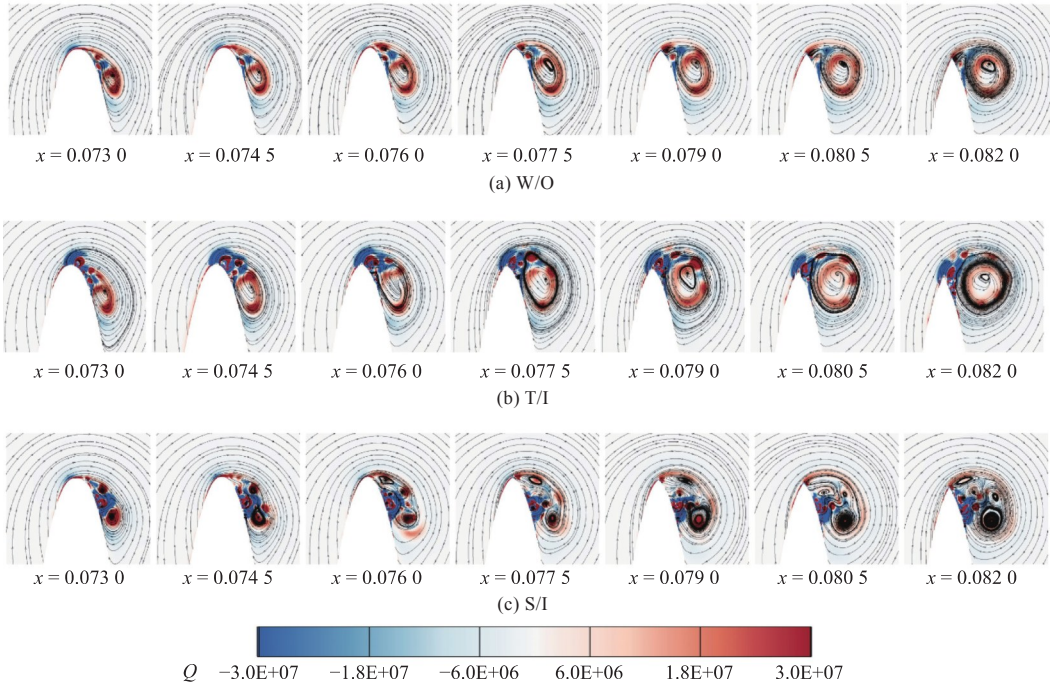

Fig. 12 Comparison of tip vortex forms under three water injection conditions

As shown in Fig. 12, the energy carried by the injected fluid will destroy the vortex structure in the nearby flow domain dramatically under both the top and side hole opening conditions. However, due to the different injection positions, the degree of damage to the vortex by the two water injection methods also varies. Under the T/I condition shown in Fig. 12(b), the injection only destroys the vortex generated at the hydrofoil tip while the tip vortex structure remains intact. Although the diameter of the tip vortex is slightly larger than that under the W/O condition, the development trend of the tip vortex is similar to that shown in Fig. 12(a). In contrast, as shown in Fig. 12(c), side injected flow can directly pass through the hydrofoil tip vortex and its cavitation core, consequently seriously deforming the tip vortex structure. The original complete vortex core is decomposed into several disordered small vortices. Under this effect, the flow disorderliness in the vortex core region increases. The directional rotation intensity of the tip vortex decreases, and the pressure drop caused by rotation decreases accordingly, ultimately suppressing the generation of hydrofoil TVC.

In addition to directly destroying the tip vortex structure, forcible changes in the trend of the rotational flow in the tip vortex also affect the cavitation in the tip vortex. As mentioned earlier, the rotation of the hydrofoil tip vortex can be divided into two parts: one is the incident flow from the pressure side of the elliptical hydrofoil, and the other is the re-entrant flow near the suction-side surface. According to the enlarged local details from the flow domain at the hole opening position shown in Fig. 12(b), the mixing of the top injected fluid can effectively change the direction and velocity of the incident flow to the tip vortex and reduce the rotation intensity of the hydrofoil tip vortex, thereby reducing the pressure drop in the vortex core. Similarly, the side injected flow also influences the re-entrant flow from the tip vortex. However, the suppression effect of this influence on the rotation intensity of the tip vortex cannot be effectively analyzed due to the severe damage to the tip vortex structure.

3.2.4 Energy analysis

The turbulent kinetic energy (TKE) is a measure of the development or attenuation of the motion of a turbulent flow. The TKE value can be used to express the intensity of the tip vortex rotation. In this study, the influence of active water injection on the tip vortex and the energy transfer during its cavitation is analyzed using the TKE and its components obtained by decomposition. The TKE transport equation is expressed as Eq. (14).

$$\frac{\mathrm{d}k}{\mathrm{d}t} = -\langle u_i' u_k' \rangle \cdot \frac{\partial \langle u_i \rangle}{\partial x_k} - \frac{\partial}{\partial x_k} \cdot \left(\frac{\langle p' u_k' \rangle}{\rho_\mathrm{m}} + \left\langle \frac{1}{2} u_i' u_i' u_k' \right\rangle - \mu_\mathrm{m} \frac{\partial k}{\partial x_k} \right) - \mu_\mathrm{m} \left\langle \frac{\partial u_i'}{\partial x_k} \cdot \frac{\partial u_i'}{\partial x_k} \right\rangle \tag{14}$$

where u_i is the velocity component; u_i' is the fluctuating velocity component; p' is the fluctuating pressure; μ_m is the dynamic viscosity; on the right side of the equal sign, the first term is the term of the TKE work, the second one is the TKE diffusion term, and the third one is the TKE dissipation term. Specifically, the TKE is measured in J, and the work term, diffusion term, and dissipation term are all measured in W according to Eq. (14).

Equation (14) demonstrates that the flow field velocity and the pressure field should be processed in a time-averaged manner in the calculation of TKE transport components. In this study, the total calculation time is 0.30 s, and the calculation stabilizes at 0.25 s. The flow field information from 0.25 to 0.30 s is selected for time-averaged statistics, namely that the statistical period is 0.05 s. Fig. 13 shows the TKE in the hydrofoil tip vortex and its components during the energy transport under three conditions. In this figure, the streamlines represent the development trend of the injected fluid from the hydrofoil. According to the analysis results of the W/O condition shown in Fig. 13(a), the TKE carried in the hydrofoil tip vortex decreases continuously as the tip vortex develops backward, which is primarily caused by the shear dissipation inside the tip vortex. The analysis results of the T/I condition shown in Fig. 13 (b) reveal that the injected fluid, carried by the tip vortex, rotates from the initial injection stage. As a result, this process increases all the TKE transport components to be higher than that under the W/O condition, with an especially salient increase in the dissipation term during the development of the tip vortex. According to the analysis results of the S/I condition shown in Fig. 13(c), the injected fluid is concentrated in the center of the tip vortex in the initial injection stage, with chaotic motion and no rotational trend for the time being. The injected fluid begins to rotate as it constantly develops backward along with the tip vortex. Moreover, the comparison of the various components in the TKE transport process shows that side injection reduces the TKE work term and increases the TKE dissipation term of the tip vortex near the injection position.

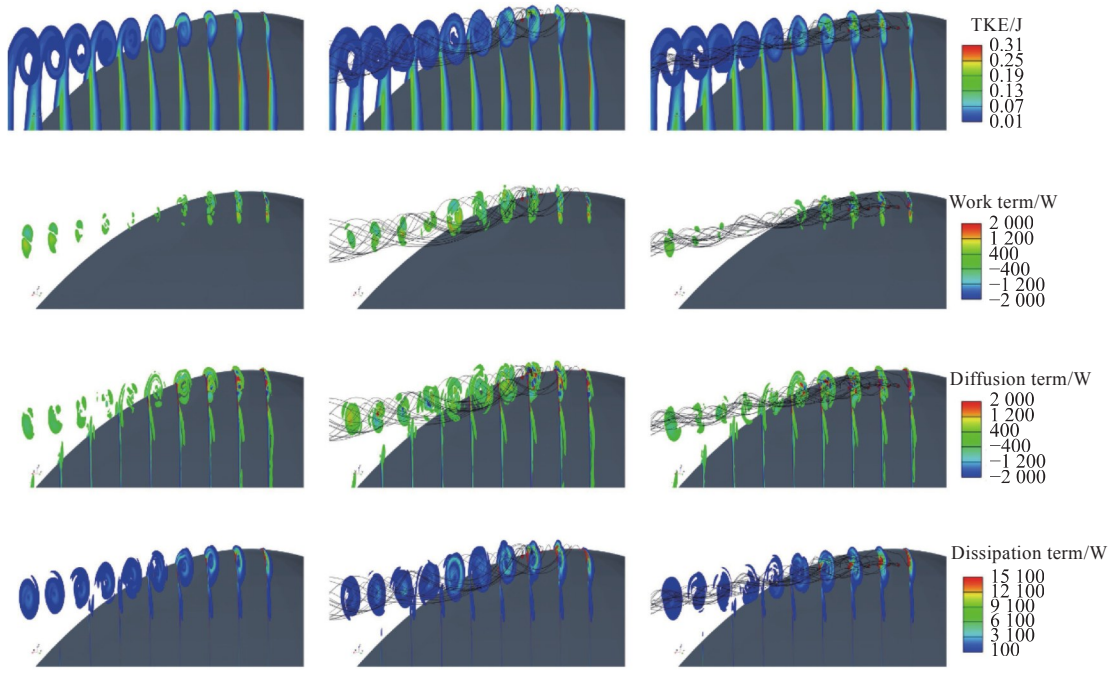

Fig. 13 Comparison of TKE components under three water injection conditions

4 Conclusions

The IDDES turbulence model and the Schnerr−Sauer cavitation model were used to simulate the tip vortex and TVC behind the NACA 0012 elliptical hydrofoil and analyze their flow characteristics under wetted flow and cavitating flow conditions. Furthermore, two active control methods, namely, top injection and side injection, were employed to control the TVC, determine the suppression effect of active water injection on hydrofoil TVC, and investigate the mechanism of this suppression effect.

1) According to the analysis of the local flow

field at the inception position of the hydrofoil tip vortex, the rotational flow in the inceptive hydrofoil tip vortex is divided into two parts: one is the incident flow to the tip vortex from the pressure side of the hydrofoil; the other is the re-entrant flow from the tip vortex converging to the suction side. In addition, the cavities compensate for the low-pressure region in the vortex core after cavitation occurs, slowing down the rotation of the hydrofoil tip vortex, increasing the diameter of the tip vortex, and changing the tip vortex from a quasi-circular shape to a quasi-elliptical shape.

2) Both the top and side active water injection methods can suppress TVC. Specifically, the latter is more effective as TVC almost no longer occurs under this condition. Although top injection also suppresses TVC, it increases the instability of the tip vortex cavities, leading to an increase in the exciting force on the hydrofoil surface.

3) The mechanism of TVC suppression by the active water injection methods is divided into two types: When the injected fluid can directly act on the tip vortex, the energy it carries destroys the tip vortex structure of the hydrofoil dramatically, decomposing the direction-fixed rotating tip vortex into several disorderly small vortices, thereby reducing the rotation of the tip vortex and suppressing the generation of TVC. When the injected fluid is far away from the tip vortex, it can still increase the TKE dissipation term of the tip vortex by changing the direction and velocity of the incident flow to the inceptive tip vortex or the re-entrant flow, thereby reducing the rotation intensity of the tip vortex.

The suppression effect of active water injection on TVC and the interaction among the injected fluid, the tip vortex, and cavitation have been verified in this study. The next step will be devoted to analyzing the influence of the injection velocity or angle on hydrofoil cavitation depending on different injection parameter settings and exploring the optimal way of suppressing TVC by water injection methods.

References

[1] LIU F Y. Numerical simulation and noise analysis of propeller tip vortex cavitation [D]. Shanghai: Shanghai Jiao Tong University, 2019 (in Chinese).

[2] CHEN K J. Numerical simulations of cavitation around hydrofoil and propeller based on OpenFOAM [D]. Shanghai: Shanghai Jiao Tong University, 2019 (in Chinese).

[3] JI B, LUO X W, ARNDT R E A, et al. Numerical simulation of three dimensional cavitation shedding dynamics with special emphasis on cavitation-vortex interaction [J]. Ocean Engineering, 2014, 87: 64−77.

[4] CHENG H Y, BAI X R, LONG X P, et al. Large eddy simulation of the tip-leakage cavitating flow with an insight on how cavitation influences vorticity and turbulence [J]. Applied Mathematical Modelling, 2020, 77: 788−809.

[5] OHTA T, SUGIURA R. Numerical prediction of interaction between turbulence structures and vortex cavitation [J]. Journal of Turbulence, 2019, 20(10): 599−625.

[6] XIE C M, LIU J Y, JIANG J W, et al. Numerical study on wetted and cavitating tip-vortical flows around an elliptical hydrofoil: Interplay of cavitation, vortices, and turbulence [J]. Physics of Fluids, 2021, 33(9): 093316.

[7] DE GIORGI M G, FICARELLA A, FONTANAROSA D. Active control of unsteady cavitating flows in turbomachinery [C]//ASME Turbo Expo 2019: Turbomachinery Technical Conference and Exposition. Phoenix, AZ, USA:ASME, 2019.

[8] KADIVAR E, TIMOSHEVSKIY M V, NICHIK M Y, et al. Control of unsteady partial cavitation and cloud cavitation in marine engineering and hydraulic systems [J]. Physics of Fluids, 2020, 32(5): 052108.

[9] WANG W, TANG T, ZHANG Q D, et al. Effect of water injection on the cavitation control: experiments on a NACA66 (MOD) hydrofoil [J]. Acta Mechanica Sinica, 2020, 36(5): 999−1017.

[10] CHANG N, GANESH H, YAKUSHIJI R, et al. Tip vortex cavitation suppression by active mass injection [J]. Journal of Fluids Engineering, 2011, 133(11): 111301.

[11] TIMOSHEVSKIY M V, ZAPRYAGAEV I I. Generation of a wall jet to control unsteady cavitation over a 2D hydrofoil: visualization and hydroacoustic signal analysis [J]. Journal of Physics: Conference Series, 2017, 899(3): 032021.

[12] LU S P, WANG W, HOU T F, et al. Experiment research on cavitation control by active injection [C]// Proceedings of the 10th International Symposium on Cavitation (CAV2018). Baltimore, MD, USA: ASME, 2018.

[13] LEE C S, AHN B K, HAN J M, et al. Propeller tip vortex cavitation control and induced noise suppression by water injection [J]. Journal of Marine Science and Technology, 2018, 23(3): 453−463.

[14] CHEN G, LI X B, LIANG X F. IDDES simulation of the performance and wake dynamics of the wind turbines under different turbulent inflow conditions [J]. Energy, 2022, 238: 121772.

[15] CAO L S, HUANG F L, LIU C, et al. Vortical structures and wakes of a sphere in homogeneous and density stratified fluid [J]. Journal of Hydrodynamics, 2021, 33(2): 207−215.

[16] WANG J B, MINELLI G, DONG T Y, et al. The effect of bogie fairings on the slipstream and wake flow of a high-speed train. an IDDES study [J]. Journal of Wind Engineering and Industrial Aerodynamics, 2019, 191: 183−202.

[17] GRITSKEVICH M S, GARBARUK A V, SCHÜTZE J, et al. Development of DDES and IDDES formulations for the k-ω shear stress transport model [J]. Flow, Turbulence and Combustion, 2012, 88(3): 431−449.

[18] SAUER J, SCHNERR G H. Development of a new cavitation model based on bubble dynamics [J]. ZAMM Journal of Applied Mathematics and Mechanics, 2001, 81(Supp 3): 561−562.

[19] YILMAZ N, ATLAR M, KHORASANCHI M. An improved mesh adaption and refinement approach to cavitation simulation (MARCS) of propellers [J]. Ocean Engineering, 2019, 171: 139−150.

[20] DE GIORGI M G, FONTANAROSA D, FICARELLA A. Characterization of unsteady cavitating flow regimes around a hydrofoil, based on an extended Schnerr-Sauer model coupled with a nucleation model [J]. International Journal of Multiphase Flow, 2019, 115: 158−180.

[21] TAKASUGI N, YAMAGUCHI H, KATO H, et al. An experiment of cavitating flow around a finite span hydrofoil [J]. Journal of the Society of Naval Architects of Japan, 1992, 1992(172): 257−265.

[22] SUN S, LI L, WANG C, et al. Numerical prediction analysis of propeller exciting force for hull-propeller rudder system in oblique flow [J]. International Journal of Naval Architecture and Ocean Engineering, 2018, 10 (1): 69−84.

基于主动射流方法的椭圆水翼梢涡空化抑制研究

刘亢[1,2], 曹留帅[1,2], 万德成*[1,2]

1 上海交通大学 船海计算水动力学研究中心,上海 200240

2 上海交通大学 船舶海洋与建筑工程学院,上海 200240

摘　要:［**目的**］梢涡空化会产生压力波动和流动噪声,预测梢涡空化的初生和发展过程,了解其作用机理并加以抑制是船舶螺旋桨与旋转机械亟待解决的问题。［**方法**］以剖面为NACA 0012 翼型的椭圆水翼为研究对象,基于IDDES 湍流模型和Schnerr-Sauer 空化模型,分别在全湿流和空泡流两种工况下对水翼梢涡及其空化现象进行模拟,分析水翼梢涡及其空化之间的相互作用特性。进一步,通过主动射流方法控制水翼梢涡空化,并对比两种开孔射流方式,即垂向射流和侧向射流的作用效果。［**结果**］以梢涡体积作为空泡抑制的判断标准,与无射流工况对比,垂向射流工况对空泡的抑制效果可达到8.09%;而在侧向射流工况下,射流对空泡的抑制效果更加明显,达到了10.47%。结果证明两种主动射流方式均可以有效抑制梢涡空化。［**结论**］通过机理分析发现,垂向射流会影响水翼梢涡入射流的流速及流向,提高梢涡湍动能的耗散项,从而降低水翼的梢涡强度;而在侧向射流工况下,射流则直接作用于梢涡,所携带的能量极大地破坏了水翼的梢涡结构,从而大大降低了梢涡空化现象的产生。

关键词: 椭圆水翼; 主动射流; 梢涡空化; IDDES; Schnerr-Sauer